NJC

Zinc stannate microcubes with integrated microheater for low-temperature NO2 detection

Journal:	*New Journal of Chemistry*
Manuscript ID	NJ-ART-06-2022-002709.R2
Article Type:	Paper
Date Submitted by the Author:	02-Aug-2022
Complete List of Authors:	Joshi, Niravkumar; University of California Berkeley, Mechanical Engineering Department Long, Hu; State Key Laboratory of Digital Manufacturing Equipment and Technology, Huazhong University of Science and Technology, Naik, Pranav; Goa University Kumar, Arvind; Chaman Lal Mahavidyalaya, Surface Engineering Division Mastelaro, Valmor; University of São Paulo, Physics Institute of São Carlos Novais Oliveira, Jr., Osvaldo; University of Sao Paulo, Physics Zettl, Alex; University of California Berkeley, Physics Lin, Liwei; University of California Berkeley, Mechanical Engineering Department

Zinc stannate microcubes with integrated microheater for low-temperature NO_2 detection

Nirav Joshi[1,2], Hu Long[3,4], Pranav Naik[5], Arvind Kumar[6], Valmor R. Mastelaro[2], Osvaldo N. Oliveira Jr[2], Alex Zettl[4], Liwei Lin[1]*

[1]Department of Mechanical Engineering, University of California, Berkeley, CA, USA

[2]São Carlos Institute of Physics, University of São Paulo, CP 369, São Carlos 13560-970, São Paulo, Brazil.

[3]Department of Mechatronics Engineering, School of Mechanical Science and Engineering, Huazhong University of Science and Technology, Wuhan, HuBei 430074, China

[4]Department of Physics, University of California at Berkeley, Materials Sciences Division, Lawrence Berkeley National Laboratory, Kavli Energy NanoSciences Institute, Berkeley, CA 94720 USA

[5]Department of Physics, Goa University, Taleigao Plateau, Goa, 403206, India.

[6]Department of Physics, Chaman Lal Mahavidyalaya, Haridwar, India.

Abstract

This paper reports a facile technique to construct an oxide nanostructured film on a low-power microheater sensor platform to detect the NO_2 gas with high sensitivity and selectivity at a low temperature. Microcube-shaped zinc stannate ($ZnSnO_3$) nanostructures prepared through a co-precipitation method were used to detect NO_2 down to 85 ppb at 110 °C with fast response and recovery time. Specifically, a 192% response in resistance change has been measured for the 5 ppm NO_2 gas with a response time of 3.36 mins, excellent reproducibility, long-term stability, and high selectivity. The good gas sensing performance of $ZnSnO_3$ microcubes is the result of its porous surface, which provides a large surface area and suitable absorption-desorption processes. The versatility of $ZnSnO_3$ nanostructures may be further exploited with various sensing units on a single chip towards the development of arrays as in electronic noses.

Keywords: Zinc Stannate; Microcubes; NO_2 sensor; Microheater; Gas Sensor

1. Introduction

Chemiresistive gas sensors made with metal oxide semiconductors (MOS) on ceramic substrates have been widely used to detect hazardous gases in industrial factories and commercial spaces to monitor air quality [1]. However, state-of-art sensors used in the fields are bulky and costly with high power consumptions (~500 mW), which makes them unsuitable for portable and battery-powered devices as a heater is needed to boost the sensitivity and response/recovery rates [2,3]. To overcome these limitations, miniaturization with microfabrication techniques has been employed to produce small and low-cost devices with low power requirements [3]. Nanostructured metal oxides with large surface areas and porous structures have been proposed to increase sensitivity, including microspheres, microcubes, and nanocages with facile adsorption-desorption processes [4–8]. The choice of nanostructured metal oxides is usually determined by the target gases. For instance, various metal oxides/binary oxides have been investigated including ZnO, SnO_2, Fe_2O_3, and Co_3O_4 [9–12]. The primary challenges with gas sensor devices are selectivity and operation temperature. Researchers are particularly interested in room temperature operation and there have been numerous attempts to increase the selectivity of these sensors. The selectivity towards a specific analyte can be enhanced by adjusting the surface-to-volume ratio, grain orientation, and film morphologies [13–15]. Other reported methods include substitutional doping, the formation of composites and hybrids with other nanomaterials such as metal oxides, 2D materials, carbon nanotubes, and so on, as well as chemical functionalization with noble metal nanoparticles. For example, Ma et al. [16] reported 3D SiO_2@MWCNT core–shell nanospheres for highly sensitive nitrogen dioxide (NO_2) gas detection at room temperature with best sensitivity of 82.61%. The response time was observed 25 min. and they used UV illumination to achieve complete recovery (44 s). Similarly, Zhang et al. [17] synthesized In_2O_3 NWs using electrospinning and reported a high sensing response of 740 at 5 ppm NO_2 in the dark at room temperature. However, they utilized visible light irradiation to shorten the recovery time (20 s). Huang et al. [18] developed a robust NO_2 sensor using SnS_2/rGO nanohybrids, showing a 650% with response time 75 s at room temperature and achieved complete recovery under visible light region. UV-light has been utilized to increase the performance of oxide and 2D materials-based gas sensors. However, UV-light degradation to the structure of the material can significantly impair reproducibility [19].

Nitrogen dioxide (NO_2) is an air pollutant with a pungent odor and high toxicity generated from fossil fuels in the combustion processes and chemical plants [15]. Overexposure to this gas can cause respiratory problems, which is particularly harmful to people with asthma [20–22]. The National Institute for Occupational Safety and Health (NIOSH) has set 1 ppm and a 15-min short-term limit as the emission standard [23]. The demand for sensitive and selective gas sensors to detect NO_2 with low power consumption has sparked sensor research with aforementioned metal oxides, but most of these materials have limitations in terms of operating temperature and selectivity [9,24,25]. Binary metal oxides are those that contain at least one transition metal ion and one or more electrochemically active/inactive ions. However, as compared to single-component oxides, binary metal oxides may have a higher redox chemical ability and may integrate contributions from two types of ions to improve sensing performance [26–28]. Zhou and co-workers [29] synthesized $ZnSnO_3$ hollow cubes with high sensitivity and selectivity for ethanol vapor detections at the ppm level at an operating temperature of 260 °C. Patil et al. [30] reported sensors made with zinc stannate films with a sensor response of 29.3 for the 40 ppm NO_2 concentration with fast response and recovery speed at an operating temperature of 200 °C. In the latter case, the room-temperature operation would be possible with the activation of chemical reactions under UV-light irradiation. Dabbabi and co-workers used $ZnSnO_3$ thin films to detect NO_2 at room temperature with fast response time but found unstable baseline resistance changes under UV light irradiation [31]. $ZnSnO_3$ has also been used for detecting volatile organic compounds (VOCs) and toxic analytes at low ppb levels, though the operation temperature is a major concern [32–35].

In this work, a simple fabrication procedure is presented for the synthesis of $ZnSnO_3$ microcubes together with a low-power microheater to yield an excellent sensing performance for the NO_2 gas. The $ZnSnO_3$ microcubes were synthesized using a co-precipitation method and a subsequent annealing process. They were deposited on a microheater platform to enhance the sensor response and selectivity for NO_2 at a low operating temperature. The improved sensing performance is attributed to the large specific surface area of the microtubes, which allows for fast gas diffusion to the active sites.

2. Experimental Section

2.1 Synthesis and Materials Characterization

$ZnSnO_3$ microcubes were synthesized using a room-temperature co-precipitation method [29]. In a typical synthesis procedure, 0.1M zinc chloride ($ZnCl_2$) and sodium citrate ($C_6H_5Na_3O_7$) were dissolved in 10 mL deionized (DI) water and the solution was added to 5 mL of a 0.2 M tin chloride ($SnCl_4$) ethanol solution under stirring to form a homogeneous solution. Then, 0.41M NaOH solution (25 mL) was added dropwise into the homogeneous solution and stirred for 1 h. White precipitates of $ZnSn(OH)_6$ were formed, washed, and centrifuged with water and ethanol for 4 times, and left to dry overnight at 80 °C. The powders were placed in a quartz tube and annealed at 450 °C for 2 h in air with heating and cooling rates of 1 °C min^{-1} to obtain $ZnSnO_3$ cubes. The synthesis procedure is schematically displayed in Figure S1 in the Supporting Information (ESI). All reagents were of analytical grade and used without further purification. The morphology of the samples was characterized using field-emission scanning electron microscopy (FE-SEM, Zeiss Sigma) operating at 5 kV, equipped with X-ray energy dispersive spectroscopy (EDS) for elemental analysis. The crystal structure was characterized using X-ray diffraction (Rigaku, Rotaflex RU-200B) with a Cu Kα target (λ = 0.15406 nm). The chemical composition and chemical state of the samples were determined with X-ray photoelectron spectroscopy (XPS) using an ESCALAB-MKII spectrometer (UK) with Al Kα radiation (1486.6 eV) as the X-ray source for excitation. The pore-size distribution and specific surface area of the samples were estimated using the Brunauer-Emmett-Teller (BET) method based on the nitrogen adsorption-desorption isotherms (BELSORP-mini II, Japan).

2.2 Sensor device fabrication and gas-sensing measurements

The gas sensors were fabricated by ultrasonically dispersing as-prepared $ZnSnO_3$ microcubes (10 mg) in 1 mL isopropyl alcohol. The suspension was then drop-cast onto the microsensor substrate containing a circularly shaped sensing area of interdigitated (line width and spacing of 20 μm) encircled by a double meandered Pt heater (line width of 50 μm) to regulate the operating temperature and ensure its uniformity as shown in **Figure 1a-b.** For the fabrication process **(Figure 1c)** [36], a 4-inch Si/SiO_2 wafer was used, and the Pt structure was patterned using standard UV Photolithography and lift-off processes. A 10 nm-thick layer of chromium and 90 nm-thick Pt were deposited by physical vapor deposition onto the wafer. The metal lift-off was performed by placing N-methyl pyrrolidone at 60-80 °C for 10 min and rinsing it with 2-propanol before drying. Each 4-inch silicon wafer contains 60-70 microsensor electrodes. The electrodes on the silicon wafer

were diced and fixed onto ceramic packages by using a conductive silver paste. The substrate has a circularly shaped sensing area of interdigitated Pt electrodes with 20 µm spacing that is encircled by a Pt heater to regulate and ensure uniformity of the operating temperature. The $ZnSnO_3$ solution was drop cast on the active area of microsensors and heated at 90°C for 15 min to evaporate the solvent, followed by calcination at 400°C in an electric furnace in the air for 2 h to stabilize the sample before the gas sensing measurements. Photos of the system are shown in Figure S2. The microsensor electrode was wire-bonded in a ceramic package and placed in a sensor chamber for electrical measurements.

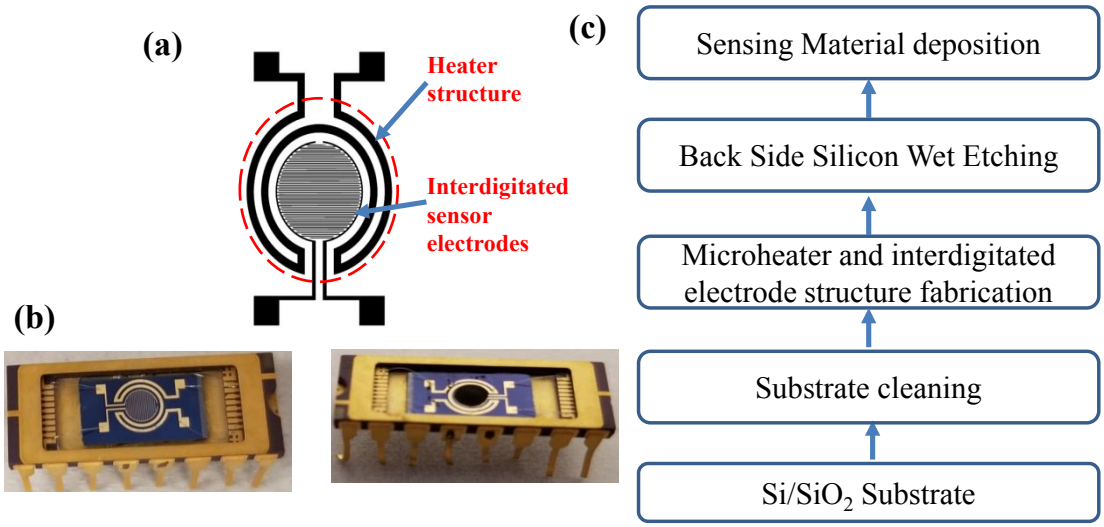

Figure 1. a) Schematic illustration of the sensor device. b) Zinc stannate microcubes with and without integrated microheater sensor (c) Microsensor Fabrication process

The $ZnSnO_3$ sensor was exposed to various gases, namely CO_2 (2000 ppm in N_2), formaldehyde (20 ppm in N_2), NO_2 (21 ppm in N_2), H_2 (5% in N_2), CO (500 ppm in N_2), which were calibrated and supplied by Praxair, Inc. A LabView-controlled gas delivery system was used to control the total flow rate of 300 sccm to the sensor chamber. The sensor signal was analyzed using a data acquisition system (Labview) with an open-source Java-based instrument (Zephyr) for controlling and obtaining the data [37–39]. The sensor measurements were conducted with a Keithley 2602 source meter by applying a bias voltage and recording the current, from which the resistance R was calculated. The gas sensing parameters obtained were the sensor response, defined as $S = (R_g - R_a)/R_a * 100$ where R_g and R_a are the resistance of the sensor film under the exposure to the test gas and fresh air, respectively. The response time (τ_{res}) is defined as the time

to reach 90% of the full response after the exposure to the target gas. The recovery time (τ_{rec}) is defined as the time to return to 10% of the baseline resistance after the target gas flow is stopped.

3. Results and discussion

3.1 Microstructural and structural characterization

Phase identification was performed using the X-ray powder diffraction (XRD) method with the diffraction pattern in **Figure 2a.** The crystal structure of $ZnSnO_3$ in **Figure 2b** was refined using the Full Proof Rietveld analysis program. The XRD data for the refinement was collected at room temperature in the 2θ range from 10 to 100° with a step size of 0.01°. Peak profiles were fitted with the pseudo-Voigt function. $ZnSnO_3$ crystals have a rhombohedral crystal symmetry in the R3c(C3v) (Space group no. 161) crystallographic point group, where the Sn atom sits at the origin [40,41]. The structural parameters from the Rietveld analysis are listed in **Table 1.** The absence of sharp peaks in the diffraction pattern indicated the presence of amorphous $ZnSnO_3$. However, the Bragg positions from Rietveld refinement were matched with JCPDS file No. 52-1381, confirming a perovskite structure without impurities. The as-prepared sample showed a pure crystalline $ZnSn(OH)_6$ in Figure S3, and this crystalline to amorphous change of the solid microcubes was observed after calcination at 450 °C for 2 h [29]. Basically, $ZnSn(OH)_6$ was dehydrated during the calcination process, and the original hydrogen-oxygen bonds in the structure were destroyed. This resulted in a large number of dangling bonds on the surface and disordering the internal lattice, thus forming amorphous $ZnSnO_3$. Because of the significant number of dangling bonds, the amorphous $ZnSnO_3$ has a larger specific surface area and exhibits superior catalytic activity compared to that of the crystallized form [42,43]. **Figure 2c** shows the N_2 adsorption-desorption isotherms for $ZnSnO_3$ microcubes, from which a specific surface area of 56.3 $m^2\ g^{-1}$ and a pore volume of 0.218 $m^3\ g^{-1}$ were calculated. The pore size distribution derived from the desorption data and estimated from the isotherm using the Barrett–Joyner–Halenda (BJH) model (inset in **Figure 2c**) indicates a pore diameter ranging from 3 to 92 nm, with an average size of 20 nm. The morphological features of the $ZnSnO_3$ sample are illustrated in **Figure 2 (d and e),** where the high and low-resolution FESEM images show uniform microcubes with an average size of 1-1.2 μm. Elemental analysis and mapping recorded in EDS analysis (Figure S4) reveal the elemental distribution of Zn, Sn, and O elements without impurities. Notably, the homogeneous dispersion of the elements was confirmed in addition to Si from the substrate.

Table 1: Structural parameters from the Rietveld analysis.

Composition	Lattice constant Å	c^2	Zn Coordinates	Sn Coordinates	O Coordinates	Cell Volume
$ZnSnO_3$	*a*=b=5.1378 c=13.4987	2.01	x=0.0000 y=0.0000 z=0.2500	x=0.000 y=0.000 z=0.000	x=0.0410 y=0.3333 z=0.0833	308.274

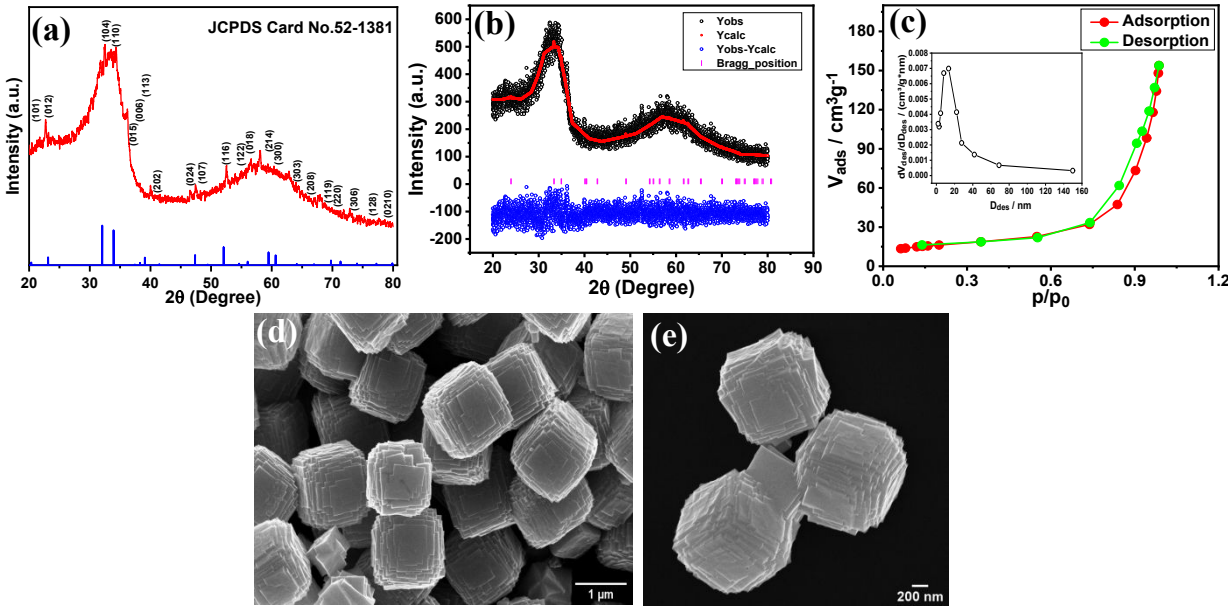

Figure 2 (a) X-ray diffractogram of as-prepared $ZnSnO_3$ microcubes; (b) Rietveld refinement of $ZnSnO_3$ sample; (c) Nitrogen adsorption-desorption isotherm of $ZnSnO_3$ microcubes; (d-e) High- and low-resolution SEM images of $ZnSnO_3$ microcubes.

The chemical states and chemical composition of $ZnSnO_3$ microcubes are depicted in the XPS spectra in **Figure 3.** The survey spectrum in **Figure 3a** reveals the presence of Zn, Sn, and O elements, without any kind of impurities. The high-resolution XPS spectra of Zn 2p, Sn 3d, and O 1s after Gaussian fitting are shown in **Figure 3 (b–d).** Two main peaks of Zn $2p_{3/2}$ and $Zn2p_{1/2}$ appear at 1021.6 and 1044.7 eV respectively in Figure 3b [44,45]. The well resolved Sn 3d spectrum in **Figure 3c** features peaks at 494.8 and 486.3 eV assigned to Sn 3d3/2 and Sn3d5/2, respectively, owing to Sn^{4+} ions [46]. **Figure 3d** shows the O 1s spectrum, which is deconvoluted into two peaks (O_I and O_{II}). The binding energy 530.6 eV for O 1s is attributed to the metal-oxygen bonding and the other peak at 532.2 eV are due to the oxygen of surface hydroxyl groups (O-H) and chemisorbed oxygen on the semiconductor [45,47,48].

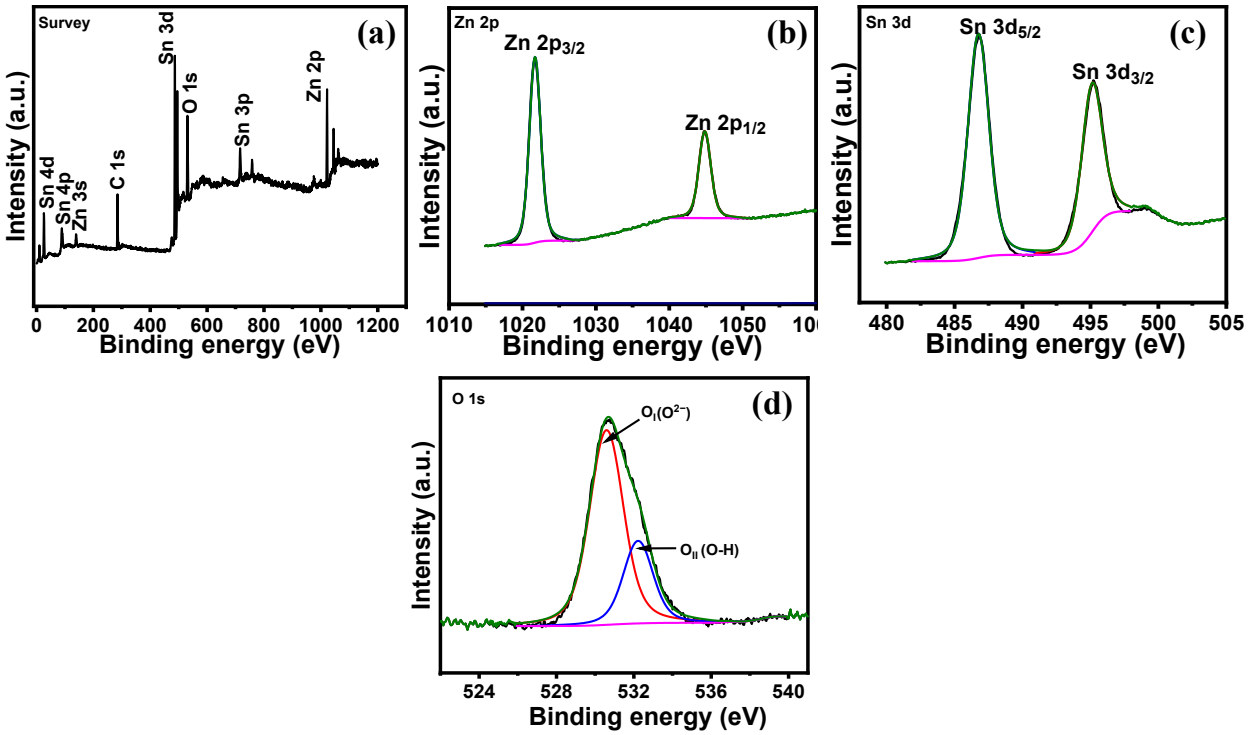

Figure 3: (a) XPS survey spectrum; (b) Zn 2p spectrum; (c) Sn 3d spectrum; (d) O 1s spectrum for the $ZnSnO_3$ microcubes.

3.2 Gas Sensing Properties

The gas-sensing performance of $ZnSnO_3$ microcubes for NO_2 gas is illustrated in **Figure 4**. The operating temperature is known to play a major role in metal oxides because it affects the sensor response/recovery speed via gas adsorption/desorption processes. **Figure 4a** shows the effect of temperature on the sensor response time for the 10 ppm NO_2 (n=4). For the $ZnSnO_3$ semiconductor, oxygen is adsorbed onto the metal oxide surfaces in the air to attract electrons from the grains forming oxygen species (O^-, O^{2-}, O_2^-, etc.) between 100 and 300°C. At low temperatures the reaction rate is low, yielding a low sensor response. With increased temperatures, the thermal energy provided is sufficient to overcome the activation energy barrier for surface reaction, which increases the reaction rate and the sensor response with respect to NO_2. Above 110 °C, the rate of desorption of chemisorbed oxygen is higher than the reaction rate, thus leading to a decline in response as observed in other works [13]. Hence, the optimum operating temperature (OT) to detect NO_2 is 110 °C. The histogram in **Figure 4b** for toxic oxidizing/reducing gases indicates significant selectivity for NO_2 owing to the rapid reaction rate of NO_2-molecules on the sensor

surface. **Figure 4c** shows sensing cycles for NO_2 at 110 °C, with increasing signals for higher concentrations. The $ZnSnO_3$ sensor displays a peak response of 342% upon the exposure to NO_2 of 10 ppm and 19% for the exposure to NO_2 of 1 ppm. **Figure 4d** shows the sensor responses of $ZnSnO_3$ microcubes with respect to the NO_2 concentration from 1 to 10 ppm at 110 ˚C (n=10). At the low concentration region, the sensor response was relatively linear before 8 ppm. This could be caused by the saturation of sites for adsorption and lack of surface adsorbed oxygen [49]. The sensor response saturates and reaches maximum after the NO_2 concentration higher than 10 ppm (as see the figure 4(d)). Moreover, the threshold limit for NO_2 gas is 10 ppm, so we varied the concentration from 1-10 ppm and due to the accuracy of the mass flow controllers in the gas delivery system, the lowest concentration of NO_2 that can be reliably delivered was 1 ppm. The limit of detection is based on the noise level during data collection, more specifically, the noise level is calculated from resistance of the sensor in air with 10 mins duration. Based on the sensor response at 1ppm, using a typical signal to noise threshold of 3, the calculated detection limit of the sensor is about 85.98 ppb. We have also confimed the reliability and stability of the sensor by performing sensing experiments until two months without any change in sensor response and film morphology (n=8).

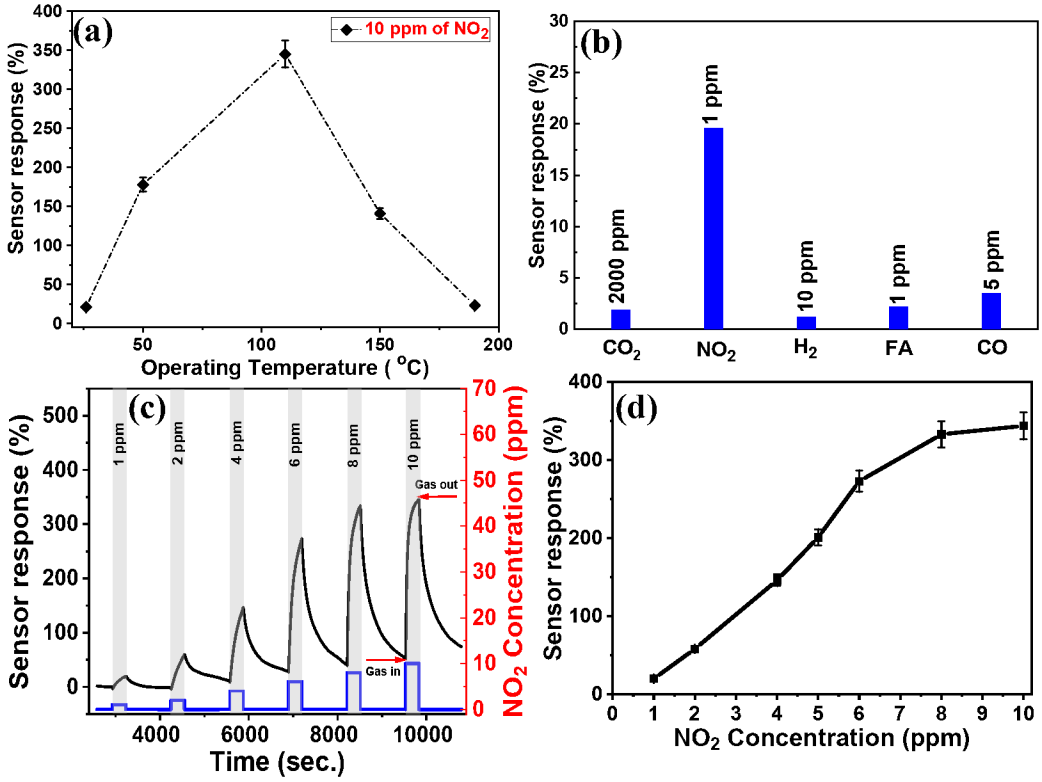

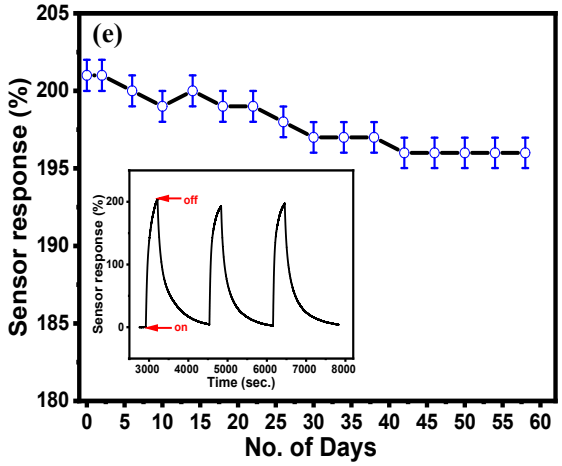

Figure 4. (a) Temperature-dependent response of the $ZnSnO_3$ sensor exposed to 10 ppm of NO_2 gas (n=4); (b) selectivity plot of $ZnSnO_3$ sensor to different oxidising and reducing gases at 110 °C; (c) dynamic sensing response for $ZnSnO_3$-based sensor to 1–10 ppm of NO_2 gas at 110 °C; (d) gas concentration-dependent sensor response of $ZnSnO_3$-based sensor to 1–10 ppm NO_2 gas at 110 °C by performing number of experiments (n=10) (e) Long-term stability tests of $ZnSnO_3$-based sensor with exposures to 5 ppm of NO_2 gas. The reproducibility of the sensor for 3 cycles of exposure to 5 ppm NO_2 is illustrated in the inset (n=8).

The long-term stability of the sensor was tested for 60 days with 5 ppm concentration of NO_2 gas at 110 °C. The results in **Figure 4e** show good stability with sensor response gradually lowering from 201% to 196% in 60 days. The reproducibility of the sensor response was confirmed with three successive cycles of NO_2 at 5 ppm with little changes. Furthermore, it is found that $ZnSnO_3$ microcubes can detect 5 ppm NO_2 with a response time of 3.36 mins while the recovery time is 11.7 mins at 110 °C as shown in Figure S5a-b. Such a high response at low temperatures is rare in the literature, as indicated in **Table 2.** The working temperature of pure $ZnSnO_3$ material was observed to be higher because the material requires more activation energy for the detection of NO_2 gas even at sub ppm levels. Heteronanostructures or surface modified zinc stannate has a higher affinity for oxidizing gases, particularly NO_2, favoring trace level detection.

Table 2. Comparison of NO_2 sensing properties for a $ZnSnO_3$ compound with other materials.

Materials	Concentration (ppm)	Sensor response	Operating Temp. (°C)	Response/Recovery time	Ref.
Zn_2SnO_4	40	29.3[a]	200	8/58 s	[30]
$ZnSnO_3$	80	12.05[b]	RT (under UV-LED)	169/217 s	[31]
Zn_2SnO_4	200	2.66[c]	200	25/326 s	[50]
Pd-Zn_2SnO_4	200	3.31[c]	200	5/179 s	[50]
Zn_2SnO_4/ZnO	1	173.26[a]	300	90/130 s	[51]
Zn_2SnO_4	1	102.21[a]	300	150/160 s	[51]
Zn_2SnO_4	5	118.45[a]	300	100/120 s	[51]
Zn_2SnO_4	5	110[b]	400	NR	[52]
rGO@Zn_2SnO_4	5	240[b]	30	NR	[52]
Pd–ZnO	1	13.5[a]	100	141/177 s	[53]
Ag–Fe_2O_3	4	3.5[a]	150	NR	[54]
Pt–WO_3	1	11.24[a]	150	27/34 s	[55]
$ZnSnO_3$	0.8	1.89[a]	125	NR	[56]
Pt- $ZnSnO_3$	0.5	16.0[a]	125	9/82 s	[56]
$ZnSnO_3$	1	19.7	110	40/140 s	This work

Response: [a](R_g/R_a), [b]$\Delta R/Ra =| Rg - Ra |/Ra$, [c]$(R_a - R_g)/R_a$ [d]Response (R_a/R_g),

3.3. Gas sensing mechanism of ZnSnO3 microcubes

The findings can be explained with a gas sensing mechanism for $ZnSnO_3$ microcubes for metal oxide gas sensors [3,35]. The mechanism for $ZnSnO_3$ microcubes and surface-depletion model for NO_2 gas is illustrated in **Figure 5.** It is a surface-controlled process regulated by the adsorption-desorption in the presence of gas molecules. $ZnSnO_3$ is a n-type semiconductor oxide in which electrons are the majority charge carriers. When the $ZnSnO_3$ microcubes are exposed to air as in **Figure 5a**, oxygen is adsorbed to form O^-_2, O^-, O^{2-} ion species by trapping/capturing electrons from the conduction band. This decreases the electrical conductivity. At the optimized operating temperature of 110 °C, adsorbed oxygen is mainly present in the O^{2-} form**. Figure 5b** shows a schematic diagram of the interaction of O_2 and NO_3 gases with the $ZnSnO_3$ grain. The reaction kinetics may be explained by the following reactions [57–59]:

$$O_{2(gas)} \rightarrow O_{2(ads.)} \quad \text{---------- (1)}$$

$$O_{2(ads.)} + e^- \rightarrow O_2^-{}_{(ads.)} \quad \text{---------- (2)}$$

$O_2^-{}_{(ads.)} + e^- \rightarrow 2O^-{}_{(ads.)}$ ---------- (3)

$O^-{}_{(ads.)} + e^- \rightarrow O^{2-}{}_{(ads.)}$ ---------- (4)

Upon the exposure to NO_2 gas, gas molecules are absorbed on $ZnSnO_3$ microcubes and act as acceptors to attract released electrons, as in the following reactions [60]:

$NO_{2\,(g)} + e^- \leftrightarrow NO_2^-{}_{(ads.)}$ ---------- (5)

$NO_2^-{}_{(ads.)} + O^{2-}{}_{(ads.)} + 2e^- \leftrightarrow NO\,(g) + 2O^{2-}{}_{(ads.)}$ ---------- (6)

A depletion region is formed on the surface of each $ZnSnO_3$ microcube as a result of these reactions, thus causing the sensor resistance to increase. When the sensors are no longer exposed to NO_2, resistance values are returned to those in the ambient air owing to a decrease in the depletion layer width and resistance. In other words, extracted electrons are returned to the conduction band, lowering the sensor resistance.

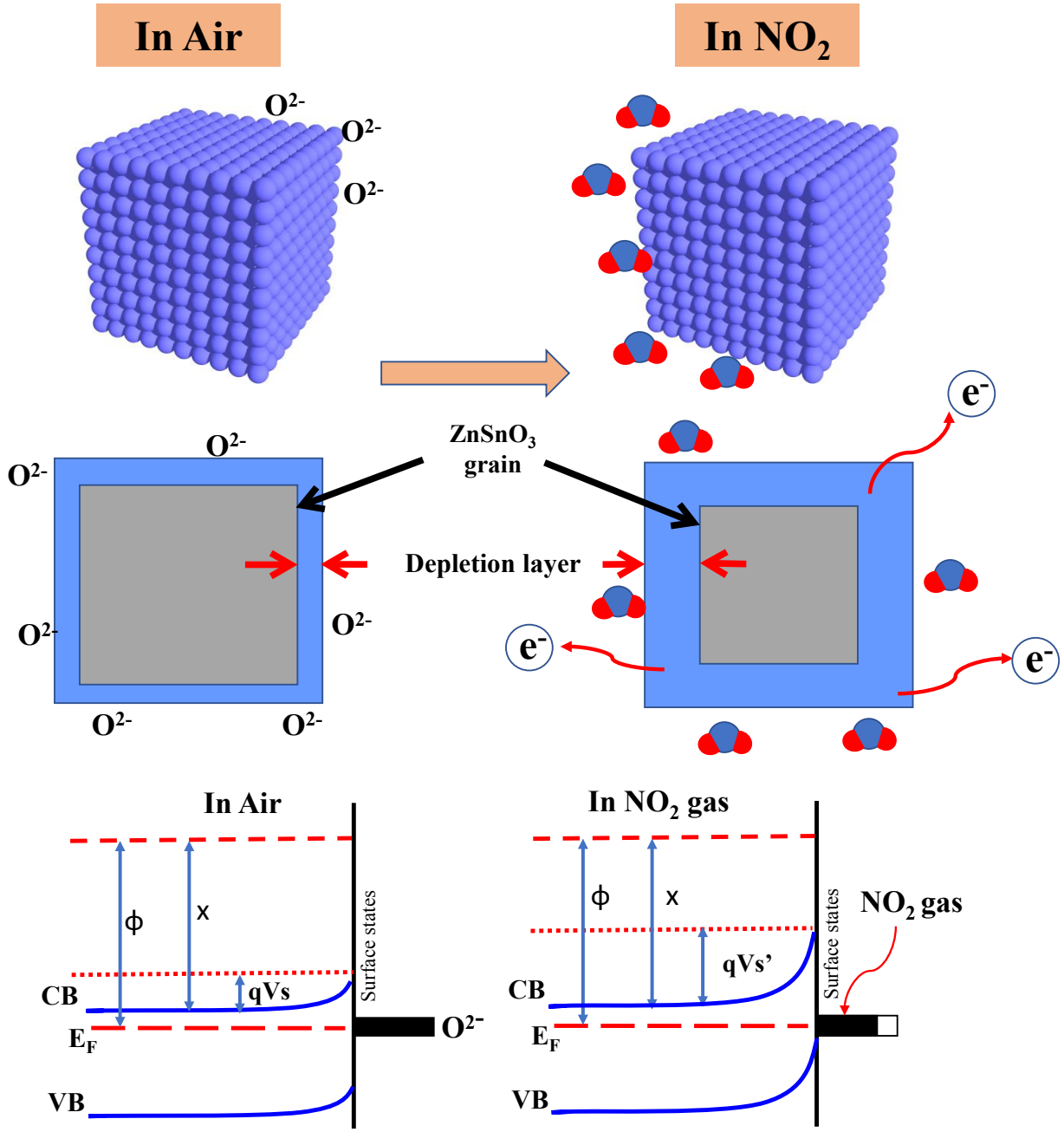

Figure 5: Schematic illustration of the NO_2 sensing mechanism of the $ZnSnO_3$ sensor.

3.4 Charge transport properties of $ZnSnO_3$ microcubes

The I-V characteristics of a $ZnSnO_3$ film at different temperatures in **Figure 6a** show the current decreases when the temperature decreases as the number of thermally generated charge carriers decreases. The change in resistance (R) with respect to temperature in **Figure 6b** allows for a linear

fitting of ln (R) vs. (1/T) in the range 300-240K, which means that the electrical conductivity of $ZnSnO_3$ film follows the Arrhenius' law $R = R_0 \exp\left(\frac{E_a}{kT}\right)$, where R_o is a constant, E_a is the activation energy, and k is the Boltzmann constant [61,62]. The activation energy was determined as ~1.7 eV using the linear portion of the curve. It is well established that the concentration of the intrinsic charge carries decreases with the decreasing temperature for semiconductors. Arrhenius' law is expected in the temperature range where intrinsic charge carriers dominate [63]. Because of defects or disordered states in the $ZnSnO_3$ film at low temperatures, the hopping transport dominates over band transport. This explains the deviation from the Arrhenius plot at low temperatures [64,65]. Taken together, these results confirm the semiconducting nature of $ZnSnO_3$ films. Moreover, the reported value of work function of Zinc stannate is 5.02-5.03 eV [66,67]. To measure the I-V and gas sensing characteristics, gold electrodes were used as the gold work function is very close to work function of Zinc stannate i.e 5.1 eV [68]. Therefore, gold can make ohmic contact with Zinc stannate.

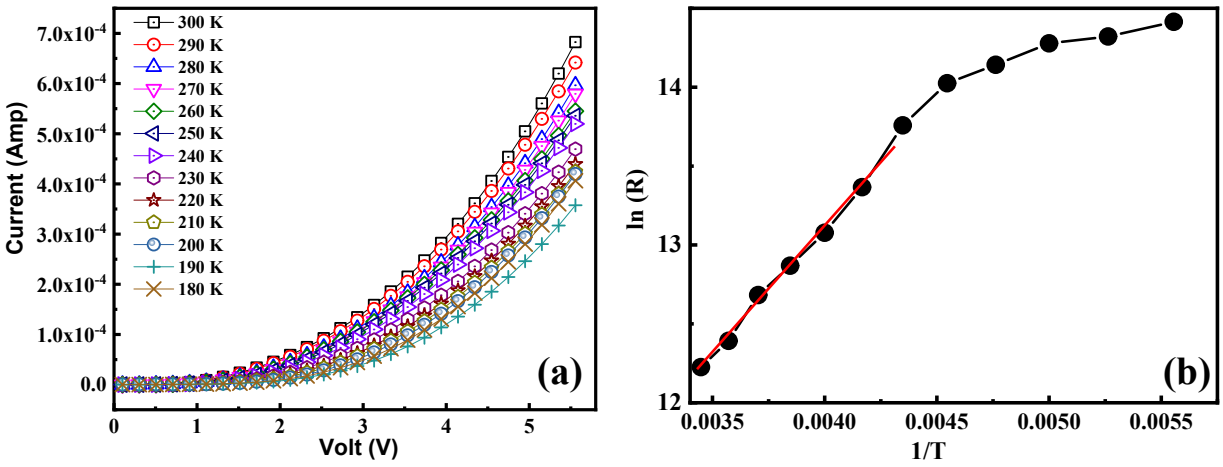

Figure 6. Temperature-dependent (a) I-V characteristics and (b) ln (R) vs (1/T) plot for a $ZnSnO_3$ film

4. Conclusion and Future Works

We have employed a simple one-step co-precipitation method to fabricate $ZnSnO_3$ microcubes for the detection of NO_2 on a low-power microheater platform. With the advantages of the large surface area of $ZnSnO_3$ nanostructures, the resulting sensor shows superior sensing response (average response of ~344 at 10 ppm) to NO_2 with fast response and recovery time at a relatively

low operating temperature of 110 °C. The sensor exhibited excellent stability for a long period of time and high selectivity to NO_2. This facile and versatile fabrication strategy provides a way to produce low-power gas sensors with low-cost mass productions. We discovered a few limitations in detecting NO_2 with this material, such as operation temperature and selectivity, and even it was observed in published articles [30–32]. The sensitivity is very low at room temperature, with a long recovery time and poor selectivity. Many researchers have used strategies such as surface modification, doping, and light illumination to overcome these issues, which we outlined in the introduction. Future approaches to $ZnSnO_3$ sensing characteristics could consider various environmental conditions and deep studies to understand the selectivity fundamentals using XPS and XRD characterization. Moreover, the interactions between the sensing layer and gas molecule will be analysed using density function theory (DFT) which will help to overcome the problem of selectivity before the actual experiment. Another possibility is to exploit the versatility of $ZnSnO_3$ and design different microsensor units with varied responses to produce an electronic nose (E-nose) on a single chip. This could permit overcoming problems of selectivity and operation temperature, as the sensing of NO_2 and other gases would be based on a global selectivity concept.

Acknowledgements

This work was supported by the Director, Office of Science, Office of Basic Energy Sciences, Materials Sciences and Engineering Division, of the U.S. Department of Energy under Contract No. DE-AC02-05-CH11231, within the van der Waals Heterostructures Program (KCWF16), which provided for gas sensor response characterization. This work was also supported in part by the Berkeley Sensor and Actuator Center (BSAC), an Industry/University Research Cooperation Center. N.J was supported by the Sao Paulo Research Foundation (FAPESP) (grant no. 2014 / 23546-1, 2016/23474-6, 2018/22214-6, 2013/07296-2) and CNPq (Brazil).

References:

[1] J. Samà, G. Domènech-Gil, I. Gràcia, X. Borrisé, C. Cané, S. Barth, F. Steib, A. Waag, J.D. Prades, A. Romano-Rodríguez, Electron beam lithography for contacting single nanowires on non-flat suspended substrates, Sensors Actuators, B Chem. (2019). https://doi.org/10.1016/j.snb.2019.01.040.

[2] S. Thomas, N. Joshi, T. Vijay, eds., Functional Nanomaterials Advances in Gas Sensing

Technologies, Springer Singapore, 2020. https://doi.org/10.1007/978-981-15-4810-9.

[3] R. Malik, V.K. Tomer, Y.K. Mishra, L. Lin, Functional gas sensing nanomaterials: A panoramic view, Appl. Phys. Rev. 7 (2020) 021301. https://doi.org/10.1063/1.5123479.

[4] R. Malik, V.K. Tomer, N. Joshi, T. Dankwort, L. Lin, L. Kienle, Au–TiO2-Loaded Cubic g-C3N4 Nanohybrids for Photocatalytic and Volatile Organic Amine Sensing Applications, ACS Appl. Mater. Interfaces. 10 (2018) 34087–34097. https://doi.org/10.1021/acsami.8b08091.

[5] N. Joshi, V.K. Tomer, R. Malik, J. Nie, Recent Advances on UV-Enhanced Oxide Nanostructures Gas Sensors, in: 2020: pp. 143–159. https://doi.org/10.1007/978-981-15-4810-9_6.

[6] N. Joshi, M.L. Braunger, F.M. Shimizu, A. Riul, O.N. Oliveira, Two-Dimensional Transition Metal Dichalcogenides for Gas Sensing Applications, in: 2020: pp. 131–155. https://doi.org/10.1007/978-3-030-38101-1_4.

[7] N. Joshi, T. Hayasaka, Y. Liu, H. Liu, O.N. Oliveira, L. Lin, A review on chemiresistive room temperature gas sensors based on metal oxide nanostructures, graphene and 2D transition metal dichalcogenides, Microchim. Acta. 185 (2018). https://doi.org/10.1007/s00604-018-2750-5.

[8] X. Chen, T. Wang, J. Shi, W. Lv, Y. Han, M. Zeng, J. Yang, N. Hu, Y. Su, H. Wei, Z. Zhou, Z. Yang, Y. Zhang, A Novel Artificial Neuron-Like Gas Sensor Constructed from CuS Quantum Dots/Bi2S3 Nanosheets, Nano-Micro Lett. (2022). https://doi.org/10.1007/s40820-021-00740-1.

[9] R. Kumar, O. Al-Dossary, G. Kumar, A. Umar, Zinc Oxide Nanostructures for NO2 Gas–Sensor Applications: A Review, Nano-Micro Lett. 7 (2015) 97–120. https://doi.org/10.1007/s40820-014-0023-3.

[10] B. Liu, Y. Luo, K. Li, H. Wang, L. Gao, G. Duan, Room-Temperature NO2 Gas Sensing with Ultra-Sensitivity Activated by Ultraviolet Light Based on SnO2 Monolayer Array Film, Adv. Mater. Interfaces. (2019). https://doi.org/10.1002/admi.201900376.

[11] P. Wang, S.Z. Wang, Q. Han, D.Q. Zou, W.K. Zhao, X.D. Wang, C. Luo, X. Yang, X.

Wu, W.F. Xie, Construction of Hierarchical α-Fe2O3/SnO2 Nanoball Arrays with Superior Acetone Sensing Performance, Adv. Mater. Interfaces. (2021). https://doi.org/10.1002/admi.202001831.

[12] V. Kruefu, U. Inpan, P. Leangtanom, C. Arkarvipath, P. Kongpark, D. Phokharatkul, A. Wisitsoraat, A. Tuantranont, S. Phanichphant, Enhanced Gas-Sensing Performances of Ru-Loaded p-Type Co3O4 Nanoparticles, Phys. Status Solidi Appl. Mater. Sci. (2018). https://doi.org/10.1002/pssa.201701015.

[13] N. Joshi, L.F. da Silva, F.M. Shimizu, V.R. Mastelaro, J.-C. M'Peko, L. Lin, O.N. Oliveira, UV-assisted chemiresistors made with gold-modified ZnO nanorods to detect ozone gas at room temperature, Microchim. Acta. 186 (2019) 418. https://doi.org/10.1007/s00604-019-3532-4.

[14] R. Malik, N. Joshi, V.K. Tomer, Advances in the designs and mechanisms of MoO3 nanostructures for gas sensors: a holistic review, Mater. Adv. 2 (2021) 4190–4227. https://doi.org/10.1039/D1MA00374G.

[15] N. Joshi, M.L. Braunger, F.M. Shimizu, A. Riul, O.N. Oliveira, Insights into nano-heterostructured materials for gas sensing: A review, Multifunct. Mater. 4 (2021) 032002. https://doi.org/10.1088/2399-7532/ac1732.

[16] D. Ma, Y. Su, T. Tian, H. Yin, T. Huo, F. Shao, Z. Yang, N. Hu, Y. Zhang, Highly Sensitive Room-Temperature NO2Gas Sensors Based on Three-Dimensional Multiwalled Carbon Nanotube Networks on SiO2Nanospheres, ACS Sustain. Chem. Eng. (2020). https://doi.org/10.1021/acssuschemeng.0c02707.

[17] B. Zhang, N. Bao, T. Wang, Y. Xu, Y. Dong, Y. Ni, P. Yu, Q. Wei, J. Wang, L. Guo, Y. Xia, High-performance room temperature NO2 gas sensor based on visible light irradiated In2O3 nanowires, J. Alloys Compd. (2021). https://doi.org/10.1016/j.jallcom.2021.159076.

[18] Y. Huang, W. Jiao, Z. Chu, G. Ding, M. Yan, X. Zhong, R. Wang, Ultrasensitive room temperature ppb-level NO2 gas sensors based on SnS2/rGO nanohybrids with P-N transition and optoelectronic visible light enhancement performance, J. Mater. Chem. C.

(2019). https://doi.org/10.1039/c9tc02436k.

[19] X. Liu, T. Ma, N. Pinna, J. Zhang, Two-Dimensional Nanostructured Materials for Gas Sensing, Adv. Funct. Mater. (2017). https://doi.org/10.1002/adfm.201702168.

[20] J.F. Grajales, A. Baquero-Bernal, Inference of surface concentrations of nitrogen dioxide (NO2) in Colombia from tropospheric columns of the ozone measurement instrument (OMI), Atmosfera. (2014). https://doi.org/10.1016/S0187-6236(14)71110-5.

[21] R. Malik, N. Joshi, V.K. Tomer, Functional graphitic carbon (IV) nitride: A versatile sensing material, Coord. Chem. Rev. 466 (2022) 214611. https://doi.org/https://doi.org/10.1016/j.ccr.2022.214611.

[22] N. Joshi, G. Pransu, C. Adam Conte-Junior, Critical review and recent advances of 2D materials-Based gas sensors for food spoilage detection, Crit. Rev. Food Sci. Nutr. (2022) 1–24. https://doi.org/10.1080/10408398.2022.2078950.

[23] No Title, (n.d.) https://www.cdc.gov/niosh/pel88/10102-44.html.

[24] J. Xuan, G. Zhao, M. Sun, F. Jia, X. Wang, T. Zhou, G. Yin, B. Liu, Low-temperature operating ZnO-based NO2sensors: A review, RSC Adv. (2020). https://doi.org/10.1039/d0ra07328h.

[25] Q. Li, W. Zeng, Y. Li, Metal oxide gas sensors for detecting NO2 in industrial exhaust gas: Recent developments, Sensors Actuators B Chem. (2022). https://doi.org/10.1016/j.snb.2022.131579.

[26] G. Ibáñez-Redín, N. Joshi, G.F. do Nascimento, D. Wilson, M.E. Melendez, A.L. Carvalho, R.M. Reis, D. Gonçalves, O.N. Oliveira, Determination of p53 biomarker using an electrochemical immunoassay based on layer-by-layer films with NiFe2O4 nanoparticles, Microchim. Acta. (2020). https://doi.org/10.1007/s00604-020-04594-z.

[27] N. Joshi, L.F. da Silva, H.S. Jadhav, F.M. Shimizu, P.H. Suman, J.-C. M'Peko, M.O. Orlandi, J.G. Seo, V.R. Mastelaro, O.N. Oliveira, Yolk-shelled ZnCo2O4 microspheres: Surface properties and gas sensing application, Sensors Actuators B Chem. 257 (2018) 906–915. https://doi.org/https://doi.org/10.1016/j.snb.2017.11.041.

[28] N. Joshi, L.F. Da Silva, H. Jadhav, J.-C. M'Peko, B.B. Millan Torres, K. Aguir, V.R. Mastelaro, O.N. Oliveira, One-step approach for preparing ozone gas sensors based on hierarchical NiCo<inf>2</inf>O<inf>4</inf> structures, RSC Adv. 6 (2016). https://doi.org/10.1039/c6ra18384k.

[29] T. Zhang, T. Zhang, R. Zhang, J. Deng, G. Lu, L. Wang, Highly sensitive sensing platform based on ZnSnO 3 hollow cubes for detection of ethanol, Appl. Surf. Sci. (2017). https://doi.org/10.1016/j.apsusc.2016.12.183.

[30] M.A. Patil, V.V. Ganbavle, K.Y. Rajpure, H.P. Deshmukh, S.H. Mujawar, Fast response and highly selective nitrogen dioxide gas sensor based on Zinc Stannate thin films, Mater. Sci. Energy Technol. (2020). https://doi.org/10.1016/j.mset.2019.11.002.

[31] S. Dabbabi, T. Ben Nasr, A. Madouri, A. Cavanna, A. Garcia-Loureiro, N. Kamoun, Fabrication and Characterization of Sensitive Room Temperature NO2 Gas Sensor Based on ZnSnO3 Thin Film, Phys. Status Solidi Appl. Mater. Sci. (2019). https://doi.org/10.1002/pssa.201900205.

[32] P. Wadkar, D. Bauskar, P. Patil, High performance H2 sensor based on ZnSnO3 cubic crystallites synthesized by a hydrothermal method, Talanta. (2013). https://doi.org/10.1016/j.talanta.2012.10.051.

[33] J. Xu, X. Jia, X. Lou, J. Shen, One-step hydrothermal synthesis and gas sensing property of ZnSnO3 microparticles, Solid. State. Electron. (2006). https://doi.org/10.1016/j.sse.2006.02.001.

[34] X. Jia, M. Tian, R. Dai, D. Lian, S. Han, X. Wu, H. Song, One-pot template-free synthesis and highly ethanol sensing properties of ZnSnO3 hollow microspheres, Sensors Actuators, B Chem. (2017). https://doi.org/10.1016/j.snb.2016.08.146.

[35] Y. Yin, F. Li, N. Zhang, S. Ruan, H. Zhang, Y. Chen, Improved gas sensing properties of silver-functionalized ZnSnO3 hollow nanocubes, Inorg. Chem. Front. (2018). https://doi.org/10.1039/c8qi00470f.

[36] A.T. Güntner, V. Koren, K. Chikkadi, M. Righettoni, S.E. Pratsinis, E-Nose Sensing of Low-ppb Formaldehyde in Gas Mixtures at High Relative Humidity for Breath Screening

of Lung Cancer?, ACS Sensors. (2016). https://doi.org/10.1021/acssensors.6b00008.

[37] Y. Wu, N. Joshi, S. Zhao, H. Long, L. Zhou, G. Ma, B. Peng, O.N. Oliveira Jr, A. Zettl, L. Lin, NO2 gas sensors based on CVD tungsten diselenide monolayer, Appl. Surf. Sci. 529 (2020) 147110. https://doi.org/10.1016/j.apsusc.2020.147110.

[38] W.S. Chi, C.S. Lee, H. Long, M.H. Oh, A. Zettl, C. Carraro, J.H. Kim, R. Maboudian, Direct Organization of Morphology-Controllable Mesoporous SnO2 Using Amphiphilic Graft Copolymer for Gas-Sensing Applications, ACS Appl. Mater. Interfaces. (2017). https://doi.org/10.1021/acsami.7b07823.

[39] H. Long, S. Turner, A. Yan, H. Xu, M. Jang, C. Carraro, R. Maboudian, A. Zettl, Plasma assisted formation of 3D highly porous nanostructured metal oxide network on microheater platform for Low power gas sensing, Sensors Actuators, B Chem. (2019). https://doi.org/10.1016/j.snb.2019.127067.

[40] H. Wang, H. Huang, B. Wang, First-principles study of structural, electronic, and optical properties of ZnSnO3, Solid State Commun. (2009). https://doi.org/10.1016/j.ssc.2009.07.009.

[41] Y. Inaguma, M. Yoshida, T. Katsumata, A polar oxide ZnSnO3 with a LiNbO3-type structure, J. Am. Chem. Soc. (2008). https://doi.org/10.1021/ja801843v.

[42] X. Wang, M. Li, B. Ding, Y. Liu, T. Chen, UV-enhanced ethanol-sensing properties of TiO2-decorated ZnSnO3 hollow microcubes at low temperature, J. Mater. Sci. Mater. Electron. (2017). https://doi.org/10.1007/s10854-017-7060-x.

[43] Q. Ge, C. Liu, Y. Zhao, N. Wang, X. Zhang, C. Feng, S. Zhang, H. Wang, W. Jiang, S. Liu, W. Ding, C. Dong, Phase evolution in preparing ZnSnO3 powders by precipitation method, Appl. Phys. A Mater. Sci. Process. (2021). https://doi.org/10.1007/s00339-020-04244-4.

[44] Q. Xie, Y. Zhao, H. Guo, A. Lu, X. Zhang, L. Wang, M.S. Chen, D.L. Peng, Facile preparation of well-dispersed CeO2-ZnO composite hollow microspheres with enhanced catalytic activity for co oxidation, ACS Appl. Mater. Interfaces. (2014). https://doi.org/10.1021/am404487b.

[45] N. Joshi, L.F. da Silva, H.S. Jadhav, F.M. Shimizu, P.H. Suman, J.-C. M'Peko, M.O. Orlandi, J.G. Seo, V.R. Mastelaro, O.N. Oliveira, Yolk-shelled ZnCo<inf>2</inf>O<inf>4</inf>microspheres: Surface properties and gas sensing application, Sensors Actuators, B Chem. 257 (2018). https://doi.org/10.1016/j.snb.2017.11.041.

[46] Y. Wang, T. Chen, Nonaqueous and template-free synthesis of Sb doped SnO2 microspheres and their application to lithium-ion battery anode, Electrochim. Acta. (2009). https://doi.org/10.1016/j.electacta.2008.11.039.

[47] D. Liu, Y. Lv, M. Zhang, Y. Liu, Y. Zhu, R. Zong, Y. Zhu, Defect-related photoluminescence and photocatalytic properties of porous ZnO nanosheets, J. Mater. Chem. A. 2 (2014) 15377–15388. https://doi.org/10.1039/C4TA02678K.

[48] A. Kumar, N. Joshi, S. Samanta, A. Singh, A.K. Debnath, A.K. Chauhan, M. Roy, R. Prasad, K. Roy, M.M. Chehimi, D.K. Aswal, S.K. Gupta, Room temperature detection of H2S by flexible gold-cobalt phthalocyanine heterojunction thin films, Sensors Actuators, B Chem. (2015). https://doi.org/10.1016/j.snb.2014.09.074.

[49] N. Joshi, L.F. Da Silva, H. Jadhav, J.C. M'Peko, B.B. Millan Torres, K. Aguir, V.R. Mastelaro, O.N. Oliveira, One-step approach for preparing ozone gas sensors based on hierarchical NiCo2O4 structures, RSC Adv. (2016). https://doi.org/10.1039/c6ra18384k.

[50] V. V. Ganbavle, M.A. Patil, H.P. Deshmukh, K.Y. Rajpure, Development of Zn2SnO4 thin films deposited by spray pyrolysis method and their utility for NO2 gas sensors at moderate operating temperature, J. Anal. Appl. Pyrolysis. (2014). https://doi.org/10.1016/j.jaap.2014.03.006.

[51] S. Park, S. An, H. Ko, C. Jin, C. Lee, Enhanced NO2 sensing properties of Zn2SnO4-core/ZnO-shell nanorod sensors, Ceram. Int. 39 (2013) 3539–3545. https://doi.org/https://doi.org/10.1016/j.ceramint.2012.10.178.

[52] V.P. Dinesh, P. Biji, Highly sensitive, graphene oxide supported zinc stannate (Zn2SnO4) nanocubes and their room temperature NO2 gas sensor properties, in: 2015 IEEE SENSORS - Proc., 2015. https://doi.org/10.1109/ICSENS.2015.7370359.

[53] X. Chen, Y. Shen, P. Zhou, S. Zhao, X. Zhong, T. Li, C. Han, D. Wei, D. Meng, NO2 sensing properties of one-pot-synthesized ZnO nanowires with Pd functionalization, Sensors Actuators, B Chem. (2019). https://doi.org/10.1016/j.snb.2018.10.063.

[54] A. Mirzaei, K. Janghorban, B. Hashemi, M. Bonyani, S.G. Leonardi, G. Neri, A novel gas sensor based on Ag/Fe2O3 core-shell nanocomposites, Ceram. Int. (2016). https://doi.org/10.1016/j.ceramint.2016.09.052.

[55] H. Liu, Y. Xu, X. Zhang, W. Zhao, A. Ming, F. Wei, Enhanced NO2 sensing properties of Pt/WO3 films grown by glancing angle deposition, Ceram. Int. (2020). https://doi.org/10.1016/j.ceramint.2020.05.236.

[56] Y. Yin, Y. Shen, S. Zhao, A. Li, R. Lu, C. Han, B. Cui, D. Wei, Enhanced detection of ppb-level NO_2 by uniform Pt-doped $ZnSnO_3$ nanocubes, Int. J. Miner. Metall. Mater. (n.d.). https://doi.org/10.1007/s12613-020-2215-9.

[57] L. Yu, F. Guo, S. Liu, B. Yang, Y. Jiang, L. Qi, X. Fan, Both oxygen vacancies defects and porosity facilitated NO2 gas sensing response in 2D ZnO nanowalls at room temperature, J. Alloys Compd. (2016). https://doi.org/10.1016/j.jallcom.2016.05.053.

[58] C. Fan, J. Shi, Y. Zhang, W. Quan, X. Chen, J. Yang, M. Zeng, Z. Zhou, Y. Su, H. Wei, Z. Yang, Fast and recoverable NO2 detection achieved by assembling ZnO on Ti3C2Tx MXene nanosheets under UV illumination at room temperature, Nanoscale. (2022). https://doi.org/10.1039/d1nr06838e.

[59] Z. Yang, W. Cao, C. Peng, T. Wang, B. Li, H. Ma, Y. Su, Z. Zhou, J. Yang, M. Zeng, Construction, Application and Verification of a Novel Formaldehyde Gas Sensor System Based on Ni-Doped SnO2Nanoparticles, IEEE Sens. J. (2021). https://doi.org/10.1109/JSEN.2021.3053407.

[60] N. Devabharathi, A.M. Umarji, S. Dasgupta, Fully Inkjet-Printed Mesoporous SnO2-Based Ultrasensitive Gas Sensors for Trace Amount NO2Detection, ACS Appl. Mater. Interfaces. (2020). https://doi.org/10.1021/acsami.0c14704.

[61] X. Li, Z.T. Song, D.L. Cai, X.G. Chen, X.L. Jia, An SPICE model for PCM based on arrhenius equation, Chinese Phys. Lett. (2009). https://doi.org/10.1088/0256-

307X/26/12/128501.

[62] A. Pirovano, A.L. Lacaita, F. Pellizzer, S.A. Kostylev, A. Benvenuti, R. Bez, Low-field amorphous state resistance and threshold voltage drift in chalcogenide materials, IEEE Trans. Electron Devices. (2004). https://doi.org/10.1109/TED.2004.825805.

[63] B. Wei, R. Spolenak, P. Kohler-Redlich, M. Rühle, E. Arzt, Electrical transport in pure and boron-doped carbon nanotubes, Appl. Phys. Lett. (1999). https://doi.org/10.1063/1.124093.

[64] C. Michel, S.D. Baranovskii, P.J. Klar, P. Thomas, B. Goldlücke, Strong non-Arrhenius temperature dependence of the resistivity in the regime of traditional band transport, Appl. Phys. Lett. (2006). https://doi.org/10.1063/1.2348771.

[65] I.P. Zvyagin, On the Theory of Hopping Transport in Disordered Semiconductors, Phys. Status Solidi. (1973). https://doi.org/10.1002/pssb.2220580203.

[66] A. Kurz, M.A. Aegerter, Novel transparent conducting sol-gel oxide coatings, Thin Solid Films. (2008). https://doi.org/10.1016/j.tsf.2007.05.082.

[67] S. Cai, Y. Li, X. Chen, Y. Ma, X. Liu, Y. He, Optical and electrical properties of Ta-doped ZnSnO3 transparent conducting films by sol–gel, J. Mater. Sci. Mater. Electron. (2016). https://doi.org/10.1007/s10854-016-4544-z.

[68] A.K. Mahapatro, S. Ghosh, Schottky energy barrier and charge injection in metal/copper-phthalocyanine/metal structures, Appl. Phys. Lett. (2002). https://doi.org/10.1063/1.1483388.